



Global ghost imaging

NIXI ZHAO,^{1,2,3} JIE TANG,^{1,2,3} CHANGZHE ZHAO,^{1,2,3} JIANWEN WU,^{1,2,3} HAN GUO,²
HAIPENG ZHANG,^{2,4} AND TIQIAO XIAO^{1,2,3,*}

¹Shanghai Institute of Applied Physics, Chinese Academy of Sciences, Shanghai 201800, China

²Shanghai Synchrotron Radiation Facility/Zhangjiang Lab, Shanghai Advanced Research Institute, Chinese Academy of Sciences, Shanghai 201204, China

³University of Chinese Academy of Sciences, Beijing 100049, China

⁴zhanghp@sari.ac.cn

*tqxiao@sari.ac.cn

Received 8 November 2024; revised 5 May 2025; accepted 19 May 2025; posted 19 May 2025; published 10 June 2025

Ghost imaging, as an imaging technique, holds great potential for standard imaging. However, the inability to achieve a large field of view, high resolution, and high-quality image reconstruction in a short time with a small number of measurements seriously hinders the practical application of ghost imaging. Parallel ghost imaging treats each pixel of the position-sensitive detector as a bucket detector and simultaneously executes tens of thousands of ghost imaging processes in parallel. This enables nonlocal imaging with high resolution, an extra-large field of view, and low dosage. In this work, we propose a dedicated imaging method for parallel ghost imaging within the framework of the bucket detector array, namely global ghost imaging. Global ghost imaging introduces global prior knowledge, enabling parallel ghost imaging not to be calculated independently within each local system but to have the global prior cover all subsystems. The speckle patterns of each ghost imaging subsystem are uploaded to the terminal for unified iterative computation. This transforms the iterative sparse solutions of each subsystem from local optima to a global optimum. Simulations and experiments demonstrate that global ghost imaging achieves a large field of view and high-resolution imaging, completely eliminates the discontinuities between subsystems, significantly improves image quality, exhibits strong noise robustness, and, more crucially, enables image reconstruction with an extremely low number of samples. By using the classical ghost imaging framework and the computational ghost imaging framework, respectively, we showcase the ability of this method to reconstruct a complex sample with an image size of 800 × 280 pixels using only eight measurements. © 2025 Optica Publishing Group under the terms of the [Optica Open Access Publishing Agreement](#)

<https://doi.org/10.1364/JOSAB.546265>

1. INTRODUCTION

Ghost imaging (GI), i.e., correlation imaging, is a new type of imaging technology based on the correlation characteristics of quantum entanglement [1,2] or classical light-field fluctuations [3–5], which can nonlocally obtain the information of the target object through the intensity correlation between the reference arm and the object arm. Ghost imaging provides a method that is difficult to obtain clear images by conventional means and can solve some problems that are not easy to solve by conventional imaging. Ghost imaging has been applied to radar detection [6,7] and optical encryption [8]. In the future, it can be further applied to fields, such as materials research [9] and life sciences [10]. GI has been proved to be suitable for classical thermal light sources [3–5]. Furthermore, it has also been proved to be suitable for atoms [11], electrons [12], neutrons [13,14], and X-rays [15–19]. Computational ghost imaging (CGI) [20] uses a spatial light modulator (SLM) to modulate the light field, eliminating the steps of recording structural illumination,

thus forming a system architecture consistent with single-pixel imaging (SPI) [21].

However, for ghost imaging, to reconstruct an image with a large field of view and high resolution, thousands of measurements are required, which is extremely time-consuming. The large number of measurements and the long experimental time have posed serious difficulties for the practical application of ghost imaging. The concept of parallel ghost imaging (PGI) was proposed by Kingston *et al.* to address this issue [13]. In this method, each pixel of the position-sensitive detector is regarded as an independent bucket detector, and tens of thousands of ghost imaging processes are carried out simultaneously in parallel during a single measurement. Kingston *et al.* and Zhang *et al.* successively implemented PGI in neutrons [13] and X-rays [22,23], respectively. After that, Sefi *et al.* [24] also achieved similar work in high-energy X-rays. Ipus *et al.* combined the parallel ghost imaging technique with the Talbot effect to reduce the number of optical elements in the optical system [25]. In our previous work, we established a true magnification between

the reference arm and the object arm through a lens, achieving high-pixel-resolution parallel imaging at the submicron level ($0.325 \mu\text{m}/\text{pixel}$), and increased the experimental efficiency from dozens of minutes to several minutes [26]. By constructing an ultra-large speckle space, we achieved ghost imaging with an ultra-large field of view of $14,000 \times 10,000$ pixels [27]. Zhao *et al.* achieved low-dose ghost imaging by using two detectors in crystal beam-splitting ghost imaging [28]. We further replaced the crystal beam-splitting with a computational ghost imaging framework and combined it with true magnification, achieving parallel ghost imaging with high pixel resolution, low dose, and a large field of view simultaneously with higher image quality [29]. Parallel ghost imaging has demonstrated great potential, and its experimental framework is gradually being expanded and improved. However, the reconstruction methods for the bucket detector array still have a large room for development.

In each single-pixel ghost imaging subsystem of parallel ghost imaging, various GI methods try their best to extract the information hidden in the signals of the two arms from various dimensions to reduce the number of measurements required for reconstructing a high-quality image. The reconstruction algorithms can be classified into three categories according to the type of iteration, including linear noniterative methods [e.g., traditional ghost imaging (TGI) [3–5], differential ghost imaging (DGI) [30], and normalized ghost imaging (NGI) [31]], linear iterative methods [e.g., gradient descent (GD)], and nonlinear iterative methods (e.g., total variation augmented Lagrangian alternating direction algorithm—TVAL3 [32]). The existing GI methods utilize the object information contained in a single subsystem to the extreme by incorporating methods, such as light intensity fluctuation correction, digital mask sorting [33,34], and compressed sensing [35,36]. On the one hand, it seems quite difficult to further reduce the number of measurements required for high-quality imaging when using the single-pixel ghost imaging method. On the other hand, all the current work simply repeatedly invokes single-pixel ghost imaging within the framework of parallel ghost imaging. This leads to discontinuities between blocks, and the iterative process of each individual block is prone to getting trapped in local optimal solutions. A set of methods specifically developed for parallel ghost imaging is necessary. Instead of repeatedly stacking single-pixel ghost imaging, which causes fragmentation, the entire image should be reconstructed through a single round of iteration.

Here, we propose global ghost imaging (GGI) from the perspective of convex optimization. GGI also adopts the parallel ghost imaging framework. Hundreds of bucket detectors are placed close to each other in the object arm to form an array, and hundreds of ghost imaging measurements are performed at the same time. This method is no longer confined to information inside the local system. The information of various dimensions and each iteration in each subsystem is shared and coordinated globally. In each iteration of each ghost imaging subsystem, not only the object information in the subsystem is the source, but also the results of all subsystems in the global domain of the previous iteration are used as a reference to jointly find the gradient statistical sparse optimal solution of the sample image globally, so that each ghost imaging subsystem is no longer in the

local optimal trap. This method not only greatly improves image quality but also reduces noise in the reconstruction results. Since the ghost imaging subsystems share the same regularization prior globally, the strong discontinuity at the junction of each subsystem is no longer generated from the underlying mechanism. The prior unification in the global domain and the interactive iterative operation between subsystems further significantly reduce the number of samples required for high-quality imaging. Simulation and experiments using the classical ghost imaging framework [23,37–40] and the computational ghost imaging framework [22] verify the ability of this method to reconstruct complex samples with 280×800 pixels in only eight measurements. This will greatly reduce the dose required for X-ray imaging and shorten the whole experimental process to 10 s or so. We believe that this research will provide a new framework for ghost imaging, which will greatly promote the practical process of ghost imaging.

2. PRINCIPLE, UNIVERSAL INTERFACE, AND SIMULATION EXPERIMENT

In the framework of the global ghost imaging experiment, each ghost imaging subsystem can be simply written as a linear system:

$$\begin{bmatrix} b_1 \\ b_2 \\ \vdots \\ b_n \end{bmatrix} = \begin{bmatrix} A(1, 1) & A(1, 2) & \cdots & A(1, m) \\ A(2, 1) & A(2, 2) & \cdots & A(2, m) \\ \vdots & \vdots & \ddots & \vdots \\ A(n, 1) & A(n, 2) & \cdots & A(n, m) \end{bmatrix} \begin{bmatrix} x_1 \\ x_2 \\ \vdots \\ x_m \end{bmatrix}, \quad (1)$$

where $A \in R^{n \times m}$ is the mask modulation matrix, that is, the speckle pattern. $x \in R^{m \times 1}$ is the object image, which is the unknown variable we need to solve. $b \in R^{n \times 1}$ is the bucket detection signal sequence. m is the number of image pixels, and n is the number of measurements. This subsystem can be abbreviated as $Ax = b$. The essence of ghost imaging is to solve a system of underdetermined linear equations. All ghost imaging methods are committed to mining the information of objects from the modulated light field A and single-pixel signal b as much as possible. In global ghost imaging, hundreds of bucket detectors are placed close to each other on the object arm, and the imaging process can be written as follows:

$$\begin{aligned} A_{1,1}x_{1,1} &= b_{1,1}; A_{1,2}x_{1,2} = b_{1,2}; \dots; A_{1,M}x_{1,M} = b_{1,M}, \\ A_{2,1}x_{2,1} &= b_{2,1}; A_{2,2}x_{2,2} = b_{2,2}; \dots; A_{2,M}x_{2,M} = b_{2,M}, \\ &\dots \\ A_{N,1}x_{N,1} &= b_{N,1}; A_{N,2}x_{N,2} = b_{N,2}; \dots; A_{N,M}x_{N,M} = b_{N,M}. \end{aligned} \quad (2)$$

The unknown variable of global ghost imaging, X , consists of $x_{1,1}, x_{1,2}, \dots, x_{n,m}$ and is a vector in ultra-high dimensional space. This framework makes it possible for GGI to reconstruct large field of view results with a very low number of measurements.

A schematic diagram of the principle of global ghost imaging is shown in Fig. 1. By taking an image with a size of 200×200 pixels as an example, where the block size is 40×40 pixels, all

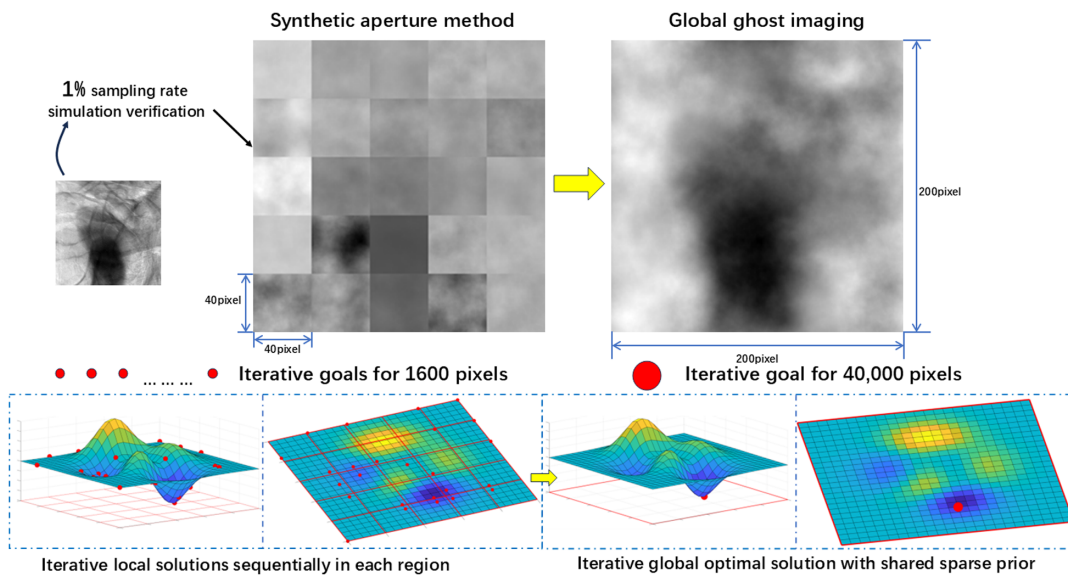


Fig. 1. Schematic diagram of global ghost imaging principle; modifying GI algorithm to implement GGI.

reconstructions are completed with 16 measurement numbers (a sampling rate of 1%). The synthetic aperture method [22,23,26] is an application of parallel ghost imaging in X-rays. In this method, the TVAL3 method is called for each block separately. The iteration of each block gets trapped in a local optimum, resulting in poor reconstruction quality. Moreover, the discontinuity between blocks seriously distorts the image. Global ghost imaging is specifically proposed for the bucket detector array. After adopting the global ghost imaging method, the quality of the imaging result is significantly improved, and the discontinuity between blocks is eliminated. This method is a concept and is not restricted to a specific algorithm. However, due to the unique bucket detector array framework of GGI, the ghost imaging algorithm cannot be directly adapted. We take TVAL3 as an example to show the principle of GGI and the method of converting a GI algorithm to GGI. TVAL3 is a nonlinear iterative algorithm based on compressed sensing counting, which can be simply expressed as

$$\begin{aligned} \text{Min} & \|c\|_{l_0} \\ \text{s.t. } & Dx = c; \\ & Ax = b, \end{aligned} \quad (3)$$

where $Ax = b$ is the measurement model of ghost imaging, D is the conversion matrix, converting the object image x to c , and l_0 norm calculates the number of nonzero elements in c and minimizes this index to find sparse solutions. The l_0 norm is a nonconvex function and is difficult to solve. It is usually approximated by the l_1 norm. TVAL3 requires fewer iterations, has strong noise robustness, and has high reconstructed image quality. It is one of the most powerful ghost imaging algorithms at present and has withstood the test of numerous experiments. When modified into a global algorithm, TVAL3 can be expressed as

$$\begin{aligned} \text{Min} & \|C\|_{l_0} \\ \text{s.t. } & DX = C; \\ & A_{1,1}x_{1,1} = b_{1,1}; \\ & A_{1,2}x_{1,2} = b_{1,2}; \\ & \dots; \\ & A_{1,M}x_{1,M} = b_{1,M}; \\ & \dots; \\ & A_{N,M}x_{N,M} = b_{N,M}. \end{aligned} \quad (4)$$

As mentioned in the GGI imaging process, X is a huge variable to be solved consisting of $x_{1,1}, x_{1,2}, \dots, x_{N,M}$. Global ghost imaging adds hundreds of ghost imaging subsystem sampling processes to the limit equation and only uses the same prior knowledge to iterate X as a whole. The augmented Lagrange method will throw $N \times M$ constraint equations onto the iteration target, so that the whole is transformed into an unrestricted equation. This is an ultra-long iteration goal with many variables, which requires a large memory space for the computer. Compared with using the single-pixel ghost imaging method to complete the reconstruction block by block, global ghost imaging requires putting the sampling data of all blocks into memory, and the memory occupied will increase multiplicatively according to the number of blocks.

Global ghost imaging liberates each ghost imaging subsystem from the local optimal iteration trap and jointly iterates to find the global optimal solution. Global ghost imaging shows powerful performance, which is stronger than all existing ghost imaging methods. We will make an extensive comparison and prove this later. However, GGI still has a small problem hindering its wide application—every GI algorithm needs to be rewritten to adapt to the GGI architecture, which is annoying and time-consuming. To address this, we propose a reverse conversion method that converts the speckle patterns of GGI into GI-adapted form, which is more efficient than previously adapting GI algorithms to GGI.

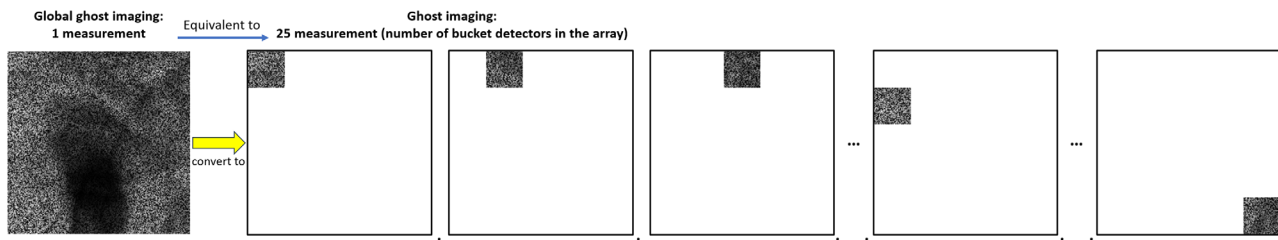


Fig. 2. More general GGI interface; reverse conversion of GGI speckle pattern to GI form.

A schematic diagram of the reverse conversion from global ghost imaging to ghost imaging is shown in Fig. 2. One measurement of global ghost imaging can be equivalently converted to $N \times M$ measurements of ghost imaging. The number of measurements increases hundreds of times while preserving a large field of view so that any GI algorithm can achieve high-quality reconstruction with a large field of view with a small number of measurements. This is equivalent to measurement number amplification technology, which provides a universal GGI-oriented interface for all GI algorithms. This will greatly reduce the use threshold of GGI and improve its versatility.

First, the performance of global ghost imaging is detected in the simulation experiment without introducing experimental error. The experimental results of a series of simulated global ghost imaging are listed in Figs. 3(a)–3(d). The target image size is 480×480 pixels. In the simulation experiment, 12×12 bucket detectors are placed in the object arm, and the image size of each ghost imaging subsystem is 40×40 pixels. In order to ensure that the simulation experiment results are not affected by the random distribution fluctuation of the speckle pattern, all simulation experiments use the same group of randomly distributed speckle patterns. The maximum number of measurements is 400, which means that for traditional single-pixel ghost imaging, the sampling rate is only 0.17%, which is hardly imageable, so it is no longer included in the comparison. We will use TGI, DGI, and TVAL3 bucket detector array ghost imaging and GGI for comparison. The measurement numbers are 100, 200, 300, and 400, respectively. The Structural Similarity Index (SSIM) is an index to evaluate the similarity between reconstruction results and objects. The comparison of SSIM values of the four methods with the number of sampling measurements is shown in Fig. 3(e).

Because of its low utilization of object information, TGI can only vaguely see the outline of the object in low-sample image reconstruction. DGI is a variant of TGI, and its effect has been improved. TVAL3 performs well in low-sampling image reconstruction and can reconstruct the object details in a single subsystem at 200 measurements. However, due to the introduction of priori in each local system, the image fragmentation caused by the discontinuity between subsystems is extremely serious. Especially in image reconstruction with a lower number of measurements (100), the image is completely torn by discontinuities. Global ghost imaging overcomes these defects. Without introducing experimental errors, the reconstruction results of images with a large field of view not only have no discontinuities between subsystems, but also the quality of reconstructed images is much higher than that of TVAL3. At 100 measurements, even if discontinuities are ignored, the

reconstruction of TVAL3 in a single subsystem is almost a complete failure. Global ghost imaging has completed the task well, and its limit is far more than that. We will discuss it again later. The SSIM value of GGI from 2 to 400 measurements is much higher than that of other methods, which strongly supports the above statement.

3. EXPERIMENTAL SETUP, SPECKLE ANALYSIS, EXPERIMENTAL RESULTS, AND RECONSTRUCTION OF ULTRA-LOW MEASUREMENT NUMBER

In response to the demand for beam-splitting in X-ray ghost imaging, we have built a crystal beam-splitting system at the X-ray testing line station BL09B [41] of the Shanghai Synchrotron Radiation Facility (SSRF) to achieve global ghost imaging in a classical framework. To achieve high-quality spatial intensity correlation beam-splitting, we have developed a crystal beam-splitter [23,37–40] specifically designed for XGI. The beam-splitter is a $300 \mu\text{m}$ thick Laue diffraction crystal developed with a diffraction Bragg angle of 5.67° . The photon energy during the experiment was 20 keV. X-rays pass through the copper foam to create a speckle pattern. The splitter divides the modulated beam into two beams in the reference arm and the object arm, with an intensity ratio of 16:1. The developed beam-splitter can achieve beam-splitting with a large field of view, and the beam-splitting correlation can reach 0.9 or above. The position-sensitive detector (OnSemi KAI-16000) will simultaneously record two beams, with the weaker beam being manually fitted into a bucket detector array. The effective area of the CCD detector is $36 \times 24 \text{ mm}^2$, with a pixel size of $7.4 \mu\text{m}$. A schematic diagram of the experimental setup is shown in Fig. 4(a).

In order to more systematically and comprehensively verify the performance of global ghost imaging, we also built a virtual beam-splitting system at the X-ray imaging and biomedical application beamline BL13HB [42] of SSRF to achieve global ghost imaging within the framework of computational ghost imaging. The modulator consists of 7 layers of 200-mesh sandpaper, and the motor carrying the sample moves in and out of the beam to record the object arm and reference arm. The bucket detector array is also artificially fitted. The photon energy during the experiment was 15 keV. The imaging system consists of a $100 \mu\text{m}$ thick scintillation crystal (LuAG: Ce), an optical conversion microscope (model: Optique Peter MICRX016), and an sCMOS detector (Hamamatsu ORCA Flash 4.0 C11440). The effective area of the detector is $6.6 \times 6.6 \text{ mm}^2$, with a pixel size of $3.25 \mu\text{m}$. The experimental setup is shown in Fig. 4(b).

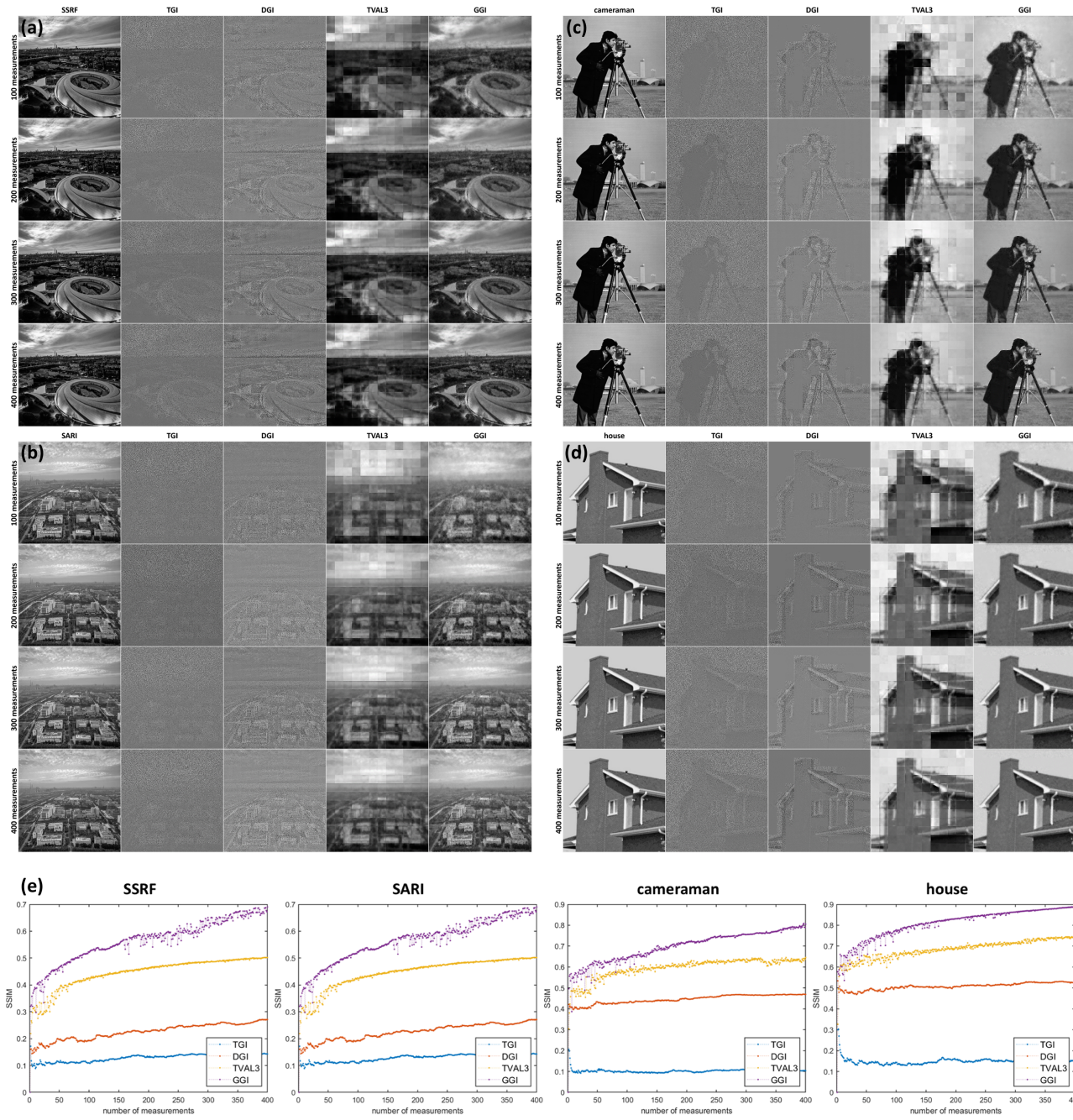
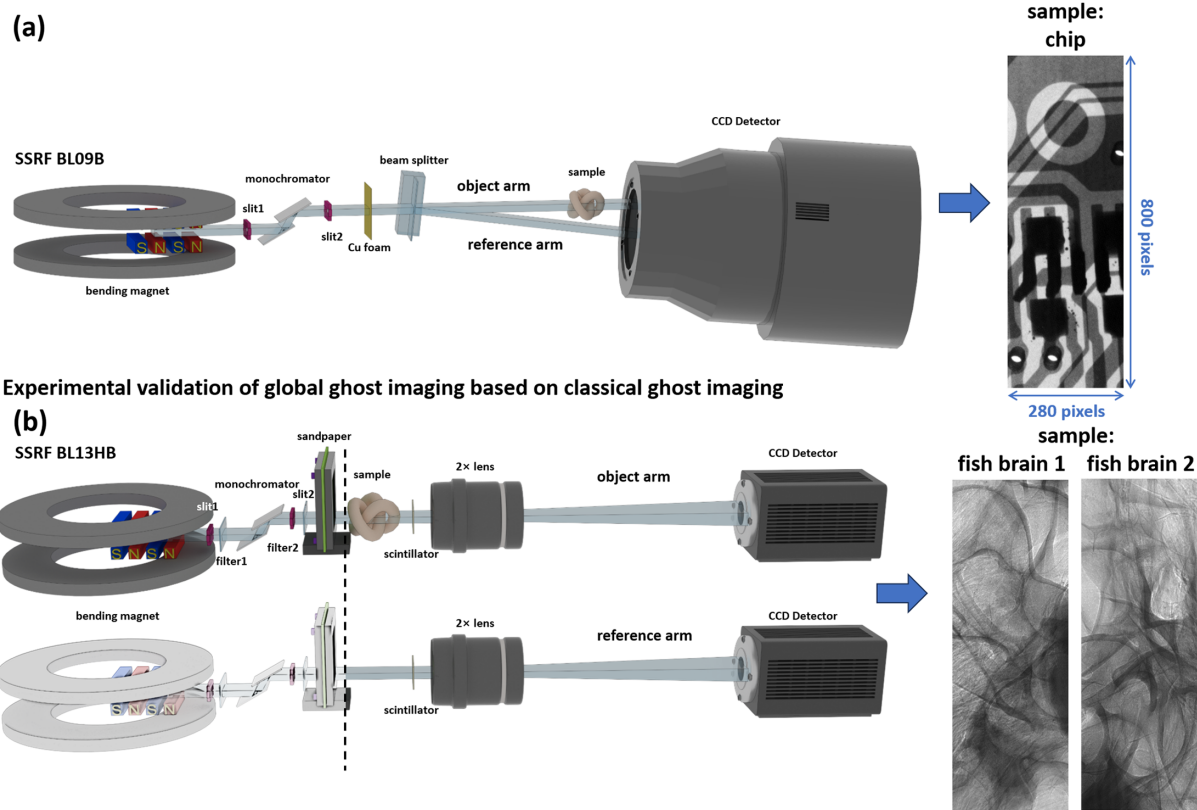


Fig. 3. Comparison of TGI, DGI, TVAL3, and GGI through simulation experiments (image size 480 × 480). The reconstruction was performed using (a) SSRF, (b) SARI, (c) cameraman, and (d) house as object images with measurements of 100, 200, 300, and 400, respectively. (e) SSIM between TGI, DGI, TVAL3, and GGI.

Because the resolution of the reconstruction results cannot be smaller than the minimum effective features of speckle patterns, speckle patterns have a decisive impact on the reconstruction quality of ghost imaging; quantification and discussion of them are necessary. For classical ghost imaging, the thickness of the modulator foam copper is about 300 μm, the aperture is between 150 and 190 μm, and the average voidage is about 77.4%. The full-width at half-maximum (FWHM) of the point-spread function (PSF) is 61.94 μm horizontally [Fig. 5(a)] and 52.45 μm vertically [Fig. 5(b)]. For calculating

ghost imaging, the hole size of the modulator sandpaper is 70 μm, and the FWHM of the PSF is 29.23 μm in the horizontal direction [Fig. 5(e)] and 29.45 μm in the vertical direction [Fig. 5(f)]. The X-ray modulation capabilities of the above two are shown in Figs. 5(d) and 5(h); the modulation ability of copper foam is stronger. The minimum effective characteristic of sandpaper is smaller than that of copper foam, but because the modulation ability of sandpaper is weaker, copper foam is more suitable for higher-energy experiments.



Experimental validation of global ghost imaging based on computational ghost imaging

Fig. 4. (a) Experimental platform for GGI based on classic ghost imaging framework at BL09B. (b) Experimental platform for GGI based on computational ghost imaging framework at BL13HB.

The quality of reconstruction results is also affected by the degree of correlation between speckle patterns. If there are speckles that can be represented by linear superposition of other speckle patterns, it is considered invalid sampling. The statistical histogram of the correlation between any combination of two speckle patterns (C_{400}^2) is shown in Figs. 5(c) and 5(g), the copper foam is more uncorrelated, and both can approximately regard the random speckle patterns as orthogonal to each other.

In the classic ghost imaging framework, we use chips as samples. In the computational ghost imaging framework, in order to challenge the ultimate ability of global ghost imaging, fish brains with high complexity and low absorption contrast were selected as samples. The object image size is 800×280 pixels, and the image size of a single ghost imaging subsystem is 40×40 pixels. The results of the experimental verification are listed in Figs. 6(a)–6(c), and the comparison graphs of SSIM values and cross-sectional lines with increasing measurement numbers are located in Fig. 6(d). Experimental results have shown that GGI using a crystal beam-splitting scheme and a virtual beam-splitting scheme both have higher imaging quality than other methods, without any discontinuity caused by independent measurements between subsystems. This enables ghost imaging to reconstruct large-sized, high-quality, and high-resolution images with fewer samples.

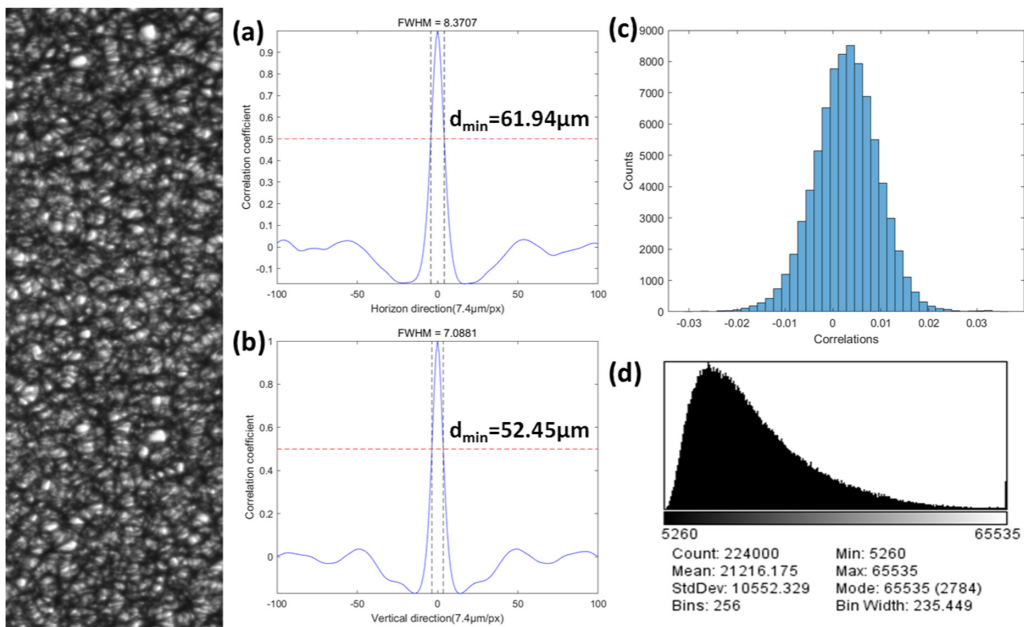
An interesting phenomenon was discovered in the experiment. Because of the short wave and strong penetration of

X-rays, the beam-splitter cannot divide the beam into two identical beams. This means that the speckle patterns of the reference arm and the object arm are not exactly the same in the classical framework, which not only leads to the inconsistency of the FWHM of the PSF in Figs. 5(a) and 5(b) but also results in poorer reconstruction quality of DGI compared to TGI only in experiments with chips as samples.

Finally, we demonstrate that GGI can reconstruct high-quality, large field of view results with only 100 measurements. Whether for a subsystem, namely traditional ghost imaging (40×40 , sampling rate 6.25%), or the entire bucket detector array (220×800 , sampling rate 0.000568%), the performance presented by GGI is astonishing. But this is far from the limit of the ability for global ghost imaging. A lower number of measurements mean a lower X-ray ionizing radiation dose and a more efficient acquisition process, which has enormous value for the practical application of ghost imaging. So we will further demonstrate the high-quality result reconstruction capability of GGI with ultra-low measurement numbers, as evidenced by Fig. 7.

Multiple sets of objects in both experimental and simulation experiments have proven that GGI can still reconstruct object images with only eight measurements! This is an ultra-low measurement count where other ghost imaging techniques have completely failed or even collapsed. Global ghost imaging provides the conditions for low-dose imaging that is hundreds

Speckle patterns of classical ghost imaging-Copper foam



Speckle patterns of computational ghost imaging-Sandpaper

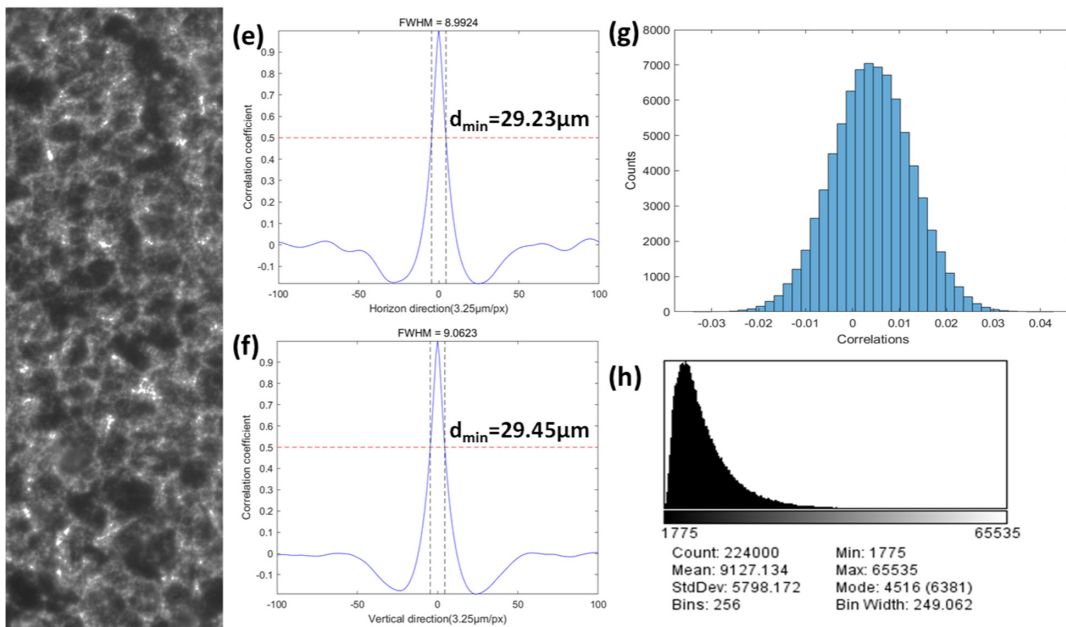


Fig. 5. Speckle analysis—copper foam and sandpaper; the FWHM of PSF in horizontal (a), (e) and vertical (b), (f) directions; (c), (g) statistical histogram of speckle pattern correlation; (d), (h) statistical histogram of speckle pattern correlation.

of times lower than X-ray standard imaging and is expected to shorten the entire experimental process to within 10 s or so.

4. CONCLUSION

Finally, it is necessary to discuss why iterative processing within the global scope yields better results than independent iterative processing within local scopes. As long as the single-pixel method is applied to the bucket detector array, regardless of the specific approach, the effect of discontinuities between blocks will inevitably occur. As far as we know, the method

that produces the least “block effect” and achieves the best reconstruction quality is to use the TVAL3 algorithm within each block. Therefore, in our discussion, we focus on why the global ghost imaging method can outperform the block-based TVAL3 algorithm. We have already fully demonstrated the effectiveness of global ghost imaging within the framework of the bucket detector array through simulations and experiments in Sections 2 and 3. Here, we provide a theoretical explanation.

The core reason for the superior performance of global ghost imaging lies in the global physical prior, which enables it to be closer to the true morphology of the sample during iteration

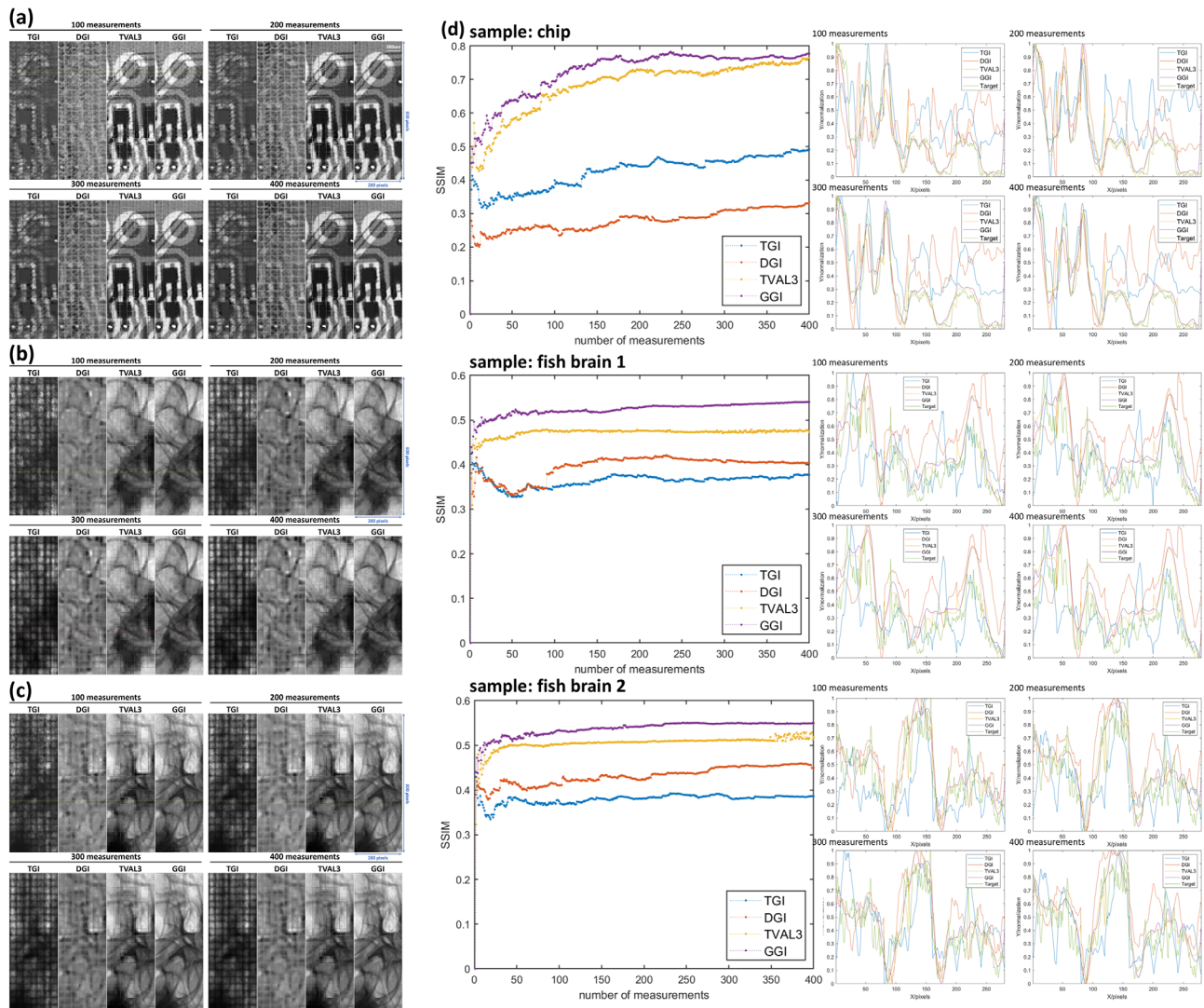


Fig. 6. Comparison of TGI, DGI, TVAL3, and GGI through experiments (image size 280×800). (a) Chip, 20 keV; (b) fish brain 1, 15 keV; (c) fish brain 2, 15 keV; (d) SSIM and cross-sectional lines of (a)–(c).

compared to other block-based priors. The physical prior of total variation (TV), in essence, aims to preserve large textures (sample contours) while smoothing out small textures (background noise). For an integrated and continuous object, its morphology should inherently have the minimum overall TV. However, when using the criterion of block-based TV, in the case of reconstructing pure background blocks without samples, background noise will be misinterpreted as samples, enhancing the noise patterns. On the other hand, for areas with strong absorption in the sample where the intensity gradient changes little, they will be regarded as noise and smoothed out. This is because the scenario best corresponding to the block-based TV criterion is when different samples are placed within each block, which mismatches the reality of a single sample. This leads to the situation that during the iterative process of block-based TV, it will not stop when the image most consistent with the sample is reached (global optimal solution) but will continue to iterate until each block becomes distinct from others and converges (local optimal solution), resulting in the appearance of block effects. We can summarize the dilemma encountered

when directly deploying the single-pixel ghost imaging method in the bucket detector array in one sentence: the smaller the total TV across the entire image, the better the reconstruction effect. Block-based TV can only make each block trapped in its own minimum TV value, and overall, the sum of TV values is actually larger, leading to worse image quality. This also explains why, even though other blocks do not detect the local area, the reconstruction quality of global ghost imaging in this local area is significantly improved—the reason is that the guidance of the global prior is more accurate.

In conclusion, we propose a global ghost imaging method and provide a way to convert conventional GI methods to GGI, as well as a simpler and more universal reverse conversion method to convert the speckle patterns of GGI into GI form. We comprehensively and systematically demonstrate through simulation experiments and experimental verification that GGI significantly improves the image quality of reconstruction results and eliminates the discontinuity between subsystems. Furthermore, we verify that global ghost imaging can also image large-sized objects at ultra-low sampling rates. Global ghost

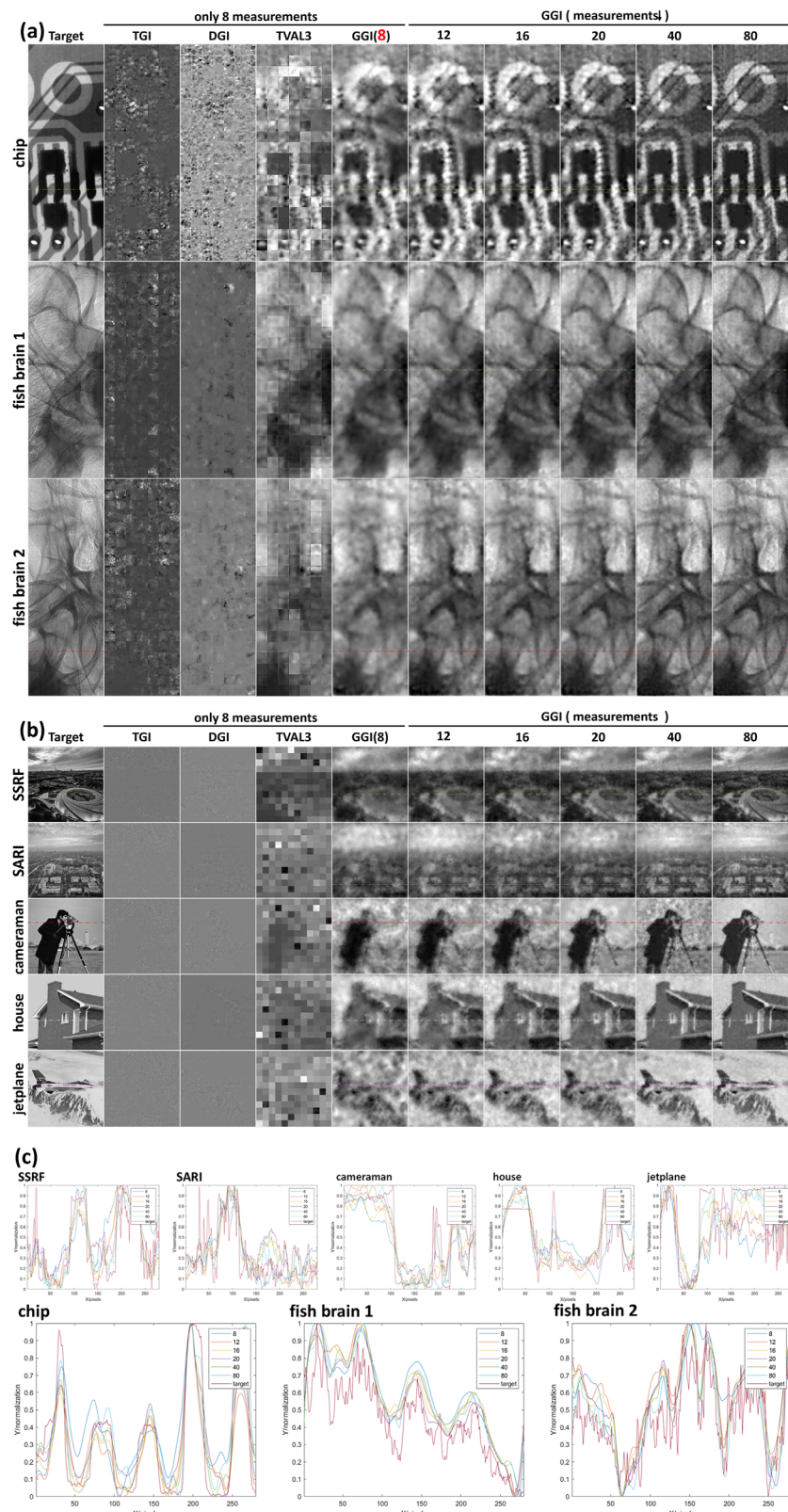


Fig. 7. Global ghost imaging reconstruction results with ultra-low measurements (only 8). (a) Experimental results, (b) simulation results, and (c) cross-sectional lines.

imaging is not limited to the framework of the bucket detector array for X-rays. We believe that it will also yield excellent results in parallel ghost imaging using neutrons, atoms, and

lasers. Since it only requires eight measurements to complete the imaging with a pixel size of 800×280 , the X-ray-based global ghost imaging holds great value for X-ray medical imaging

(digital radiography). It has extremely high practical value, deep scalability, and broad application prospects. We believe that this study provides a new framework for ghost imaging, which will greatly accelerate the practical process of ghost imaging.

Funding. National Key Research and Development Program of China (2022YFA1603601, 2021YFF0601203, 2021YFA1600703); Young Scientists Fund of the National Natural Science Foundation of China (12205361).

Acknowledgment. The authors thank WenJie Hao, Kang Du, Zenghao Song, JunXiong Fang, YanLing Xue, Ke Li, and FeiXiang Wang for their kind help and fruitful discussion on experiments and data processing.

Disclosures. The authors declare no conflicts of interest.

Data availability. Data underlying the results presented in this paper are not publicly available at this time but may be obtained from the authors upon reasonable request.

REFERENCES

- T. B. Pittman, Y. Shih, D. Strekalov, et al., "Optical imaging by means of two-photonics quantum entanglement," *Phys. Rev. A* **52**, R3429 (1995).
- D. Strekalov, A. Sergienko, D. Klyshko, et al., "Observation of two-photonics 'ghost' interference and diffraction," *Phys. Rev. Lett.* **74**, 3600 (1995).
- R. S. Bennink, S. J. Bentley, and R. W. Boyd, "Two-photonics' coincidence imaging with a classical source," *Phys. Rev. Lett.* **89**, 113601 (2002).
- A. Valencia, G. Scarcelli, M. D'Angelo, et al., "Two-photonics imaging with thermal light," *Phys. Rev. Lett.* **94**, 063601 (2005).
- F. Ferri, D. Magatti, A. Gatti, et al., "High-resolution ghost image and ghost diffraction experiments with thermal light," *Phys. Rev. Lett.* **94**, 183602 (2005).
- N. D. Hardy and J. H. Shapiro, "Computational ghost imaging versus imaging laser radar for three-dimensional imaging," *Phys. Rev. A* **87**, 023820 (2013).
- S. Ma, Z. Liu, C. Wang, et al., "Ghost imaging LiDAR via sparsity constraints using push-broom scanning," *Opt. Express* **27**, 13219–13228 (2019).
- P. Clemente, V. Durán, V. Torres-Company, et al., "Optical encryption based on computational ghost imaging," *Opt. Lett.* **35**, 2391–2393 (2010).
- F. Wang, W. Hua, C. Zhao, et al., "Small angle X-ray scattering ghost imaging," *Phys. Rev. Res.* **6**, 043293 (2024).
- X.-H. Zhu, Y.-F. Bai, W. Tan, et al., "High-resolution microscopic ghost imaging for bioimaging," *Phys. Rev. Appl.* **20**, 014028 (2023).
- R. I. Khakimov, B. Henson, D. Shin, et al., "Ghost imaging with atoms," *Nature* **540**, 100–103 (2016).
- S. Li, F. Cropp, K. Kabra, et al., "Electron ghost imaging," *Phys. Rev. Lett.* **121**, 114801 (2018).
- A. M. Kingston, G. R. Myers, D. Pelliccia, et al., "Neutron ghost imaging," *Phys. Rev. A* **101**, 053844 (2020).
- Y.-H. He, Y.-Y. Huang, Z.-R. Zeng, et al., "Single-pixel imaging with neutrons," *Sci. Bull.* **66**, 133–138 (2021).
- H. Yu, R. Lu, S. Han, et al., "Fourier-transform ghost imaging with hard X rays," *Phys. Rev. Lett.* **117**, 113901 (2016).
- D. Pelliccia, A. Rack, M. Scheel, et al., "Experimental x-ray ghost imaging," *Phys. Rev. Lett.* **117**, 113902 (2016).
- A. Schori and S. Schwartz, "X-ray ghost imaging with a laboratory source," *Opt. Express* **25**, 14822–14828 (2017).
- D. Pelliccia, M. P. Olbinado, A. Rack, et al., "Towards a practical implementation of X-ray ghost imaging with synchrotron light," *IUCrJ* **5**, 428–438 (2018).
- A. Schori, D. Borodin, K. Tamasaku, et al., "Ghost imaging with paired x-ray photonics," *Phys. Rev. A* **97**, 063804 (2018).
- J. H. Shapiro, "Computational ghost imaging," *Phys. Rev. A Atomic Mol. Opt. Phys.* **78**, 061802 (2008).
- M. F. Duarte, M. A. Davenport, D. Takhar, et al., "Single-pixel imaging via compressive sampling," *IEEE Signal Process Mag.* **25** (2), 83–91 (2008).
- H. Zhang, K. Li, F. Wang, et al., "Megapixel X-ray ghost imaging with a binned detector in the object arm," *Chin. Opt. Lett.* **20**, 033401 (2022).
- C.-Z. Zhao, H.-P. Zhang, J. Tang, et al., "X-ray ghost imaging with a specially developed beam splitter," *Synchrotron Radiat.* **31**, 1525–1533 (2024).
- O. Sefi, A. Ben Yehuda, Y. Klein, et al., "20 μm resolution multi-pixel ghost imaging with high-energy x-rays," *Opt. Express* **32**, 37001–37010 (2024).
- E. Ipus, A. J. Lenz, V. Duran, et al., "Block-based single-pixel imaging by means of the Talbot effect," *Opt. Lett.* **50**, 2105–2108 (2025).
- N. Zhao, J. Tang, C. Zhao, et al., "Synthetic aperture X-ray ghost imaging with sub-micron pixel resolution," *Opt. Express* **33**, 972–982 (2025).
- N. Zhao, J. Tang, C. Zhao, et al., "Parallel ghost imaging with extra large field of view and high pixel resolution," *ChinaXiv* (2025).
- C. Zhao, J. Tang, N. Zhao, et al., "Megapixel X-ray ghost imaging using a bucket detector array to reduce the cumulative exposure," *ChinaXiv* (2025).
- N. Zhao, J. Tang, C. Zhao, et al., "Parallel ghost imaging with ultra low dose and high pixel resolution," *ChinaXiv* (2025).
- F. Ferri, D. Magatti, L. Lugiato, et al., "Differential ghost imaging," *Phys. Rev. Lett.* **104**, 253603 (2010).
- B. Sun, S. S. Welsh, M. P. Edgar, et al., "Normalized ghost imaging," *Opt. Express* **20**, 16892–16901 (2012).
- C. Li, W. Yin, H. Jiang, et al., "An efficient augmented Lagrangian method with applications to total variation minimization," *Comput. Optim. Appl.* **56**, 507–530 (2013).
- Z. Zhou, S.-G. Li, Q.-S. Tan, et al., "Optimization method of hadamard coding plate in γ-ray computational ghost imaging," *Nucl. Sci. Tech.* **34**, 13 (2023).
- H. Zhang, K. Du, C. Zhao, et al., "Optimizing the ordering of the Hadamard masks of ghost imaging suitable for the efficient face reconstruction using the max-projection method," *Sci. Rep.* **13**, 22702 (2023).
- D. L. Donoho, "Compressed sensing," *IEEE Trans. Inf. Theory* **52**, 1289–1306 (2006).
- H. Zhang, K. Li, C. Zhao, et al., "Efficient implementation of x-ray ghost imaging based on a modified compressive sensing algorithm," *Chin. Phys. B* **31**, 064202 (2022).
- Z. Hai-Peng, Z. Chang-Zhe, J. Xiao-Lu, et al., "Improving quality of crystal diffraction based X-ray ghost imaging through iterative reconstruction algorithm," *Acta Phys. Sin.* **71** (2022).
- Z. Chang-Zhe, S. Shang-Yu, Z. Hai-Peng, et al., "Beam splitting characteristics of crystal X-ray Laue diffraction," *Acta Phys. Sin.* **71** (2022).
- C.-Z. Zhao, S.-Y. Si, Q.-S. Diao, et al., "Development of stress-free Laue diffraction crystal for x-ray beam splitting," *Proc. SPIE* **13069**, 328–334 (2024).
- C.-Z. Zhao, S.-Y. Si, H.-P. Zhang, et al., "Intensity correlation properties of x-ray beams split with Laue diffraction," *Chin. Phys. B* **33**, 014102 (2024).
- Z. Li, Y. Fan, L. Xue, et al., "The design of the test beamline at SSRF," in *Proceedings Of The 13th International Conference On Synchrotron Radiation Instrumentation-SRI2018* (2019).
- J.-F. Ji, H. Guo, Y.-L. Xue, et al., "The new X-ray imaging and biomedical application beamline BL13HB at SSRF," *Nucl. Sci. Tech.* **34**, 197 (2023).